Research Square

Preprints are preliminary reports that have not undergone peer review.
They should not be considered conclusive, used to inform clinical practice,
or referenced by the media as validated information.

Local Morphology Controls Fano Output Zeros and Nonlinear Chirality in Gold Helicoids

Gursoy B Akguc

gursoy.akguc@ieu.edu.tr

İzmir University of Economics

Orion Chiftja

Prairie View A&M University

Research Article

Keywords: chiral nanophotonics, plasmonic helicoids, Fano interference, output zeros, second-harmonic generation, multipolar radiation

Posted Date: November 17th, 2026

DOI: https://doi.org/10.21203/rs.3.rs-11625694/v1

License: This work is licensed under a Creative Commons Attribution 4.0 International License.
Read Full License

Additional Declarations: No competing interests reported.

Local Morphology Controls Fano Output Zeros and Nonlinear Chirality in Gold Helicoids

Gürsoy Bozkurt Akgüç[1,2,*], Orion Ciftja[2]

[1]Department of Physics, Izmir University of Economics, Izmir, Türkiye

[2]Department of Physics, Prairie View A&M University, Prairie View, Texas, USA

[*]Corresponding author: gursoy.akguc@ieu.edu.tr

Abstract

Local changes to a chiral metal nanoparticle can alter its radiation without substantially shifting its principal resonances. We investigate this distinction in connected gold helicoids by varying the winding of one four-groove face while retaining the other five faces and the left-handed backbone. Full-wave electromagnetic simulations are combined with complex angular-channel and vector-spherical-harmonic decompositions, Argand trajectories, singular-value analysis, and a reduced pole/output-zero description. In the 560–610 nm band, a dominant mixed-multipolar channel interferes with a weaker predominantly electric-octupolar branch, producing fixed-channel amplitude minima and rapid phase rotation. The fitted pole positions vary modestly, while local face winding reorganizes the interference and circular dissymmetry. A two-step surface second-harmonic-generation calculation separates nonlinear source formation from radiation at the generated frequency. At a generated wavelength of 600 nm, the radiated dissymmetry changes from -0.131 to $+0.986$, whereas the nonlinear-source-norm dissymmetry remains below 0.09. For the counter-wound face, a source-norm ratio of 1.092 corresponds to a radiated-power ratio of 2.944. Mesh-refinement tests support the stability of the principal linear and nonlinear results. These findings identify local face winding as a control parameter for plasmonic interference and support a phase-sensitive, generated-frequency interpretation of nonlinear chiroptical amplification beyond scalar source-strength enhancement.

Keywords: chiral nanophotonics; plasmonic helicoids; Fano interference; output zeros; second-harmonic generation; multipolar radiation

1 Introduction

Three-dimensional chiral plasmonic nanoparticles provide a direct structural route to polarization-selective excitation and radiation at dimensions well below the wavelength. Peptide- and amino-acid-directed growth has produced gold helicoids with strong visible chiroptical response and a continuously connected three-dimensional morphology [1]. Subsequent size-control studies showed that their spectral response can be tuned substantially without abandoning the characteristic helicoidal form [2, 3], while single-particle scatterometry and photothermal circular-dichroism measurements demonstrated that ensemble spectra can conceal particle-to-particle variations and morphology-dependent chiroptical behavior [4, 5]. Gold helicoids have also been extended beyond passive size tuning, for example through magnetic modulation of their plasmonic chirality [6].

Recent work reinforces the importance of multipolar composition rather than a single scalar-resonance picture. Geometry-dependent circular-dichroism reversal in bichiral gold nanoparticles has been traced to changes in multipolar excitation, including an important electric-quadrupolar contribution [7]. Helicoidal Au@Cu_2O core–shell particles likewise exhibit enriched chiroptical spectra associated with coupled electric and magnetic multipoles [8]. These observations motivate a description in which local winding changes amplitudes, phases, and radiation weights of overlapping channels even when the gross particle size changes little. We therefore introduce a geometric *face-helicity coordinate h* that modifies only one selected face while the left-handed helicoid backbone and the other five faces are retained.

The nonlinear response provides a complementary probe because second-harmonic generation (SHG) separates naturally into formation of a complex source at the pump frequency and propagation of that source through the electromagnetic response at 2ω. Chiroptical hyper-Rayleigh scattering has been measured from individual Au helicoids in solution [9], and helicoid-III particles show pronounced second-harmonic optical circular dichroism [10]. More broadly, nonlinear chirality has been demonstrated through SHG circular dichroism, optical rotation, and higher-multipolar source engineering [11–14]. A recent broadband study of plasmonic nanohelices further showed strong wavelength- and geometry-dependent SH chiroptical scattering [15]. For centrosymmetric metals, surface-SHG models construct a nonlinear polarization from the fundamental field and propagate the resulting complex source at 2ω [16, 17]. A large SH dissymmetry therefore need not imply a comparably large imbalance in scalar pump enhancement or in the integrated magnitude of the nonlinear source.

The same distinction is essential for Fano interference. A peak, dip, or sign reversal in an intensity-derived g factor is not by itself evidence for Fano physics. Fano responses arise from coherent amplitudes with different phase evolution contributing to the same output [18–21]. Chiral plasmonic Fano coupling can alter optical chirality [22], and nonlinear plasmonic studies have shown that Fano interference can reshape and enhance frequency-converted signals [23, 24], while coupled plasmonic assemblies can also produce substantial nonlinear chiro-optical amplification [25]. The experimentally observed output zero can move independently of pole locations, making complex fields and channel-resolved phase information particularly valuable.

Here we use a one-face perturbation as a local design variable on an otherwise fixed three-dimensional chiral resonator. Scalar cross sections are combined with complex angular fields, full-sphere multipoles, driven-current overlaps, numerical refinement, finite-angle collection, and a two-step surface-SHG calculation that separates pump-field solution, nonlinear-source formation, and radiation at 2ω. In the structured 560–610 nm band, a dominant mixed-multipolar radiation channel interferes with a weaker predominantly electric-octupolar branch, producing an amplitude minimum, rapid phase rotation, and fourfold angular redistribution. The central result is that a localized morphological change reorganizes phase-sensitive radiative cancellation and circular dissymmetry while the fitted resonance poles remain comparatively stable. In the nonlinear response, the same local control produces near-unity SHG dissymmetry while the scalar nonlinear-source imbalance remains comparatively weak. This establishes a nanoscale structure–function principle in which local winding and connectivity tune coherent channel weights and output zeros, with the generated-frequency radiation environment acting as a nonlinear chiroptical amplifier rather than requiring wholesale redesign of the nanostructure.

2 Computational Model

Full-wave electromagnetic calculations were performed using COMSOL Multiphysics 6.4 with the Wave Optics Module. The reference geometry is a nominally 160 nm left-handed gold helicoid-III surrogate with four curved grooves on each of six faces. The connected version extends groove mouths to the rounded edges so neighboring-face current pathways are not artificially interrupted. The helicoid backbone and five unmodified faces remain left-handed throughout the series. Only one selected face is varied according to

$$\theta_m(t) = \theta_{m,0} + h\Theta s(t), \qquad m = 0, 1, 2, 3, \tag{1}$$

where $\Theta \simeq 58^\circ$ is the left-handed reference face winding and $s(t)$ is the common radial profile. Thus $h = +1$ retains the left-handed reference face, $h = +0.5$ reduces that left-handed winding, $h = 0$ gives a radial selected face, $h = -0.5$ gives a partial right-handed counter-winding, and $h = -1$ reverses only that face to a right-handed winding while the rest of the particle remains left-handed. Throughout this work, "face helicity" denotes this geometric winding coordinate and not the electromagnetic helicity of the field. The five-state path is intended as a controlled mechanistic interpolation rather than an optimization sweep over helicoid morphology. This one-face perturbation also provides a controlled model of local morphological variability: growth, truncation, etching, or local overgrowth can modify one region of a three-dimensional helicoid while leaving most of its chiral backbone intact. Varying only the selected face therefore tests whether a localized structural modification can substantially tune chiroptical response without redesigning the entire particle. As shown below, such a local perturbation can strongly reweight coherent radiation channels even when the principal resonance positions move only modestly. Figure 1 summarizes the geometry, mesh, polarization convention, and two principal spectral regions.

A separate topology-control family retains grooves that terminate before the rounded edges rather than connecting neighboring faces. For the $h = +1$ reference, this change leaves the polarization-averaged scattering peak nearly unchanged (0.2171 μm^2 at 720 nm for the contained geometry and 0.2139 μm^2 at 730 nm for the connected geometry) while substantially reorganizing g_{sca}. This shows that edge connectivity primarily modifies helicity-selective coherent interference rather than merely increasing the overall plasmonic scattering strength. Supporting Information (Online Resource 1), Sec. S5.3 illustrates the contained reference/radial/counter-wound geometries together with the shallow edge-touching $D = 0.25$ control and summarizes their scattering response.

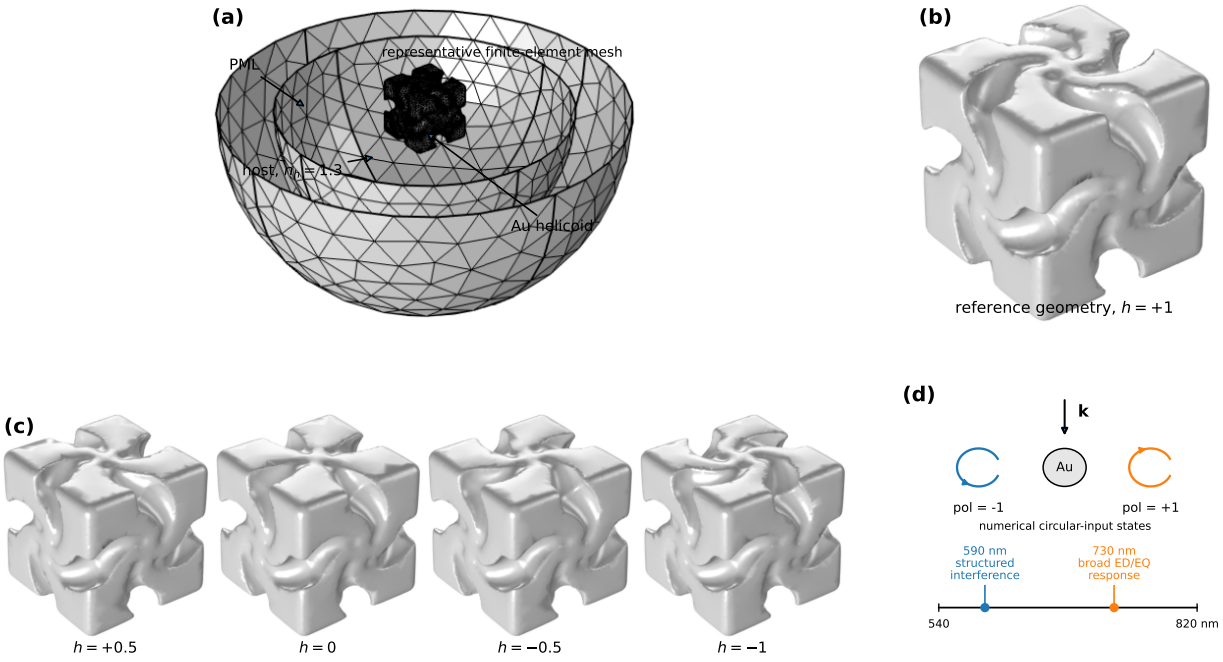


Fig. 1 Geometry, computational model, and spectral landmarks. (a) Computational domain and representative mesh. (b) Reference left-handed connected helicoid with $h = +1$. (c) Modified-face geometries $h = +0.5, 0, -0.5, -1$, for which only the selected face is progressively unwound and then right-handed counter-wound. (d) Circular-polarization states used in the calculations, together with the structured 590-nm interference region and broad 730-nm response.

The particle is embedded in a homogeneous medium of refractive index $n_h = 1.3$. The nominal spherical far-field and outer perfectly matched layer radii are 400 and 550 nm from the particle center, respectively. Linear calculations cover 540–820 nm. The SHG calculation uses pump wavelengths $\lambda_\omega = 1080$–1640 nm and reports generated wavelengths $\lambda_{2\omega} = \lambda_\omega/2 = 540$–$820$ nm.

The incident background field is

$$\widetilde{\boldsymbol{E}}_{\mathrm{inc}}(z) = \frac{E_{\mathrm{amp}}}{\sqrt{2}}\,(\hat{\boldsymbol{x}} + \mathrm{i}\,\mathtt{pol}\,\hat{\boldsymbol{y}})\,e^{-\mathrm{i}n_h k_0 z}, \tag{2}$$

with propagation along $+z$. With the harmonic convention used in the model, $\boldsymbol{E}(\boldsymbol{r},t) = \mathrm{Re}[\widetilde{\boldsymbol{E}}(\boldsymbol{r})e^{\mathrm{i}\omega t}]$, and the optical convention in which handedness is assigned while looking toward the source, i.e. against the propagation direction, we define

$$\sigma \equiv \mathtt{pol}, \qquad \sigma = -1\ (\mathrm{LCP}), \qquad \sigma = +1\ (\mathrm{RCP}). \tag{3}$$

The numerical `pol` label is retained where useful for reproducibility, while LCP/RCP and σ are used in the physical discussion.

For every positive scalar observable Q we use

$$g_Q = 2\frac{Q_{\mathrm{LCP}} - Q_{\mathrm{RCP}}}{Q_{\mathrm{LCP}} + Q_{\mathrm{RCP}}}. \tag{4}$$

To resolve the coherent radiation channels, 361 samples on the equatorial far-field circle cover $0 \le \phi \le 2\pi$ and the duplicated endpoint is removed. With circle normal $\hat{\boldsymbol{z}}$ and reference direction $\hat{\boldsymbol{x}}$,

$$E_\phi = -E_x^{\mathrm{far}} \sin\phi + E_y^{\mathrm{far}} \cos\phi, \tag{5}$$

$$E_\theta = -E_z^{\mathrm{far}}. \tag{6}$$

The vector field is expanded as

$$\boldsymbol{e}(\phi, \lambda) = \sum_m \boldsymbol{c}_m(\lambda) e^{\mathrm{i}m\phi}. \tag{7}$$

A second export samples the full sphere. The tangential field is expanded in vector spherical harmonics, following standard electromagnetic multipole practice [26],

$$\boldsymbol{E}_{\mathrm{far}}(\theta, \phi) = \sum_{\ell m} \left[a_{\ell m}^{(E)} \boldsymbol{\Psi}_{\ell m} + a_{\ell m}^{(M)} \boldsymbol{\Phi}_{\ell m} \right], \tag{8}$$

using composite-Simpson quadrature in θ, periodic quadrature in ϕ, and a discrete Gram correction. The principal analysis uses $\ell_{\max} = 8$; the worst weighted RMS reconstruction error over all 390 geometry/polarization/wavelength states is 1.42×10^{-4}.

Numerical stability is tested by comparing the production Normal mesh with a physics-controlled Fine mesh for the $h = 0$ structured band, while a 1-nm sweep from 575 to 605 nm tests spectral resolution. The equivalent induced current inside gold relative to the host is

$$\boldsymbol{J}_{\mathrm{ind}} = \mathrm{i}\omega\epsilon_0(\epsilon_{\mathrm{Au}} - \epsilon_h)\boldsymbol{E}, \qquad \epsilon_h = n_h^2 = 1.69, \tag{9}$$

with the Johnson–Christy response used in the material model [27]. On the common $z = 50$ nm cut plane the normalized complex current overlap is

$$C_J(\lambda_1, \lambda_2) = \frac{\int_A \boldsymbol{J}^*(\lambda_1) \cdot \boldsymbol{J}(\lambda_2)\, dA}{\sqrt{\int_A |\boldsymbol{J}(\lambda_1)|^2 dA \int_A |\boldsymbol{J}(\lambda_2)|^2 dA}}. \tag{10}$$

Finite collection is obtained by direct integration of the stored full-sphere field over cones about $\pm z$. The definitions and complete collection-angle dependence are given in Supporting Information Sec. S14.

For the nonlinear calculations, gold is treated with an effective surface nonlinear polarization. The implemented source retains the tangential surface term

$$\boldsymbol{P}_s^{(2)}(2\omega) = \epsilon_0 \chi_{tnt}^{(2)} E_n \boldsymbol{E}_t, \tag{11}$$

where $E_n = \boldsymbol{n} \cdot \boldsymbol{E}_\omega$ and $\boldsymbol{E}_t = \boldsymbol{E}_\omega - E_n \boldsymbol{n}$ are evaluated from the gold-side pump field. This is a restricted effective surface model, not an extraction of the full gold surface tensor; analogous tangential surface terms are used in earlier helicoid and noble-metal SHG calculations [10, 17].

The pump field at frequency ω is solved and stored independently for each incident circular polarization. Those pump fields are then used to construct the effective surface polarization in equation (11), which serves as the source for a separate electromagnetic solution at 2ω. The pump-to-SH transfer is explicitly indexed by pump wavelength and polarization so that every nonlinear calculation uses the intended stored pump state. The implementation-specific source expressions, indexed solution retrieval, validation of the pump-to-SH

transfer, and radiated-power closure tests are documented in Supporting Information Sec. S16, with the numerical workflow summarized in Sec. S23.

The total radiated SH power is obtained from the time-averaged Poynting flux through the far-field surface,

$$P_{2\omega}^{(s)} = \int_{S_{\mathrm{FF}}} \left\langle \boldsymbol{S}_{2\omega}^{(s)} \right\rangle \cdot \hat{\boldsymbol{n}}\, dS, \tag{12}$$

with upper and lower surface partitions used for directional checks. Their sum reproduces the total radiated power to numerical precision.

To distinguish source formation from radiation, we define the full-surface source norm

$$S_P^{(s)} = \int_{S_{\mathrm{Au}}} \left(|P_{sx,\mathrm{SH}}^{(s)}|^2 + |P_{sy,\mathrm{SH}}^{(s)}|^2 + |P_{sz,\mathrm{SH}}^{(s)}|^2 \right) dS, \tag{13}$$

and a complex source–field overlap diagnostic

$$O_{\mathrm{SH}}^{(s)} = \int_{S_{\mathrm{Au}}} \boldsymbol{E}_{2\omega}^{(s)*} \cdot \boldsymbol{P}_{s,\mathrm{SH}}^{(2,s)}\, dS. \tag{14}$$

We form g_P from S_P using equation (4), and use

$$g_{|O|} = 2\frac{|O_{\mathrm{SH}}^{(\mathrm{LCP})}| - |O_{\mathrm{SH}}^{(\mathrm{RCP})}|}{|O_{\mathrm{SH}}^{(\mathrm{LCP})}| + |O_{\mathrm{SH}}^{(\mathrm{RCP})}|} \tag{15}$$

only as a diagnostic. Because $\boldsymbol{E}_{2\omega}$ is itself the response to the source, O_{SH} is not an independent modal coupling coefficient.

3 Results and Discussion

3.1 Linear chiroptical response and Fano interference

The complete connected-face series cannot be described by translating or rescaling a single line shape. In the validated production spectra, the strongest negative scattering branch occurs for the partially right-handed selected face, with $g_{\mathrm{sca}} = -0.2749$ at 585 nm for $h = -0.5$, while the fully counter-wound state is nearly as strong, $g_{\mathrm{sca}} = -0.2730$ at 585 nm for $h = -1$. The positive branch is likewise non-monotonic: its largest value in the five-state sequence is +0.1169 at 610 nm for $h = 0$, rather than at either endpoint. The $h = 0$ selected face is locally unwound while the complete three-dimensional particle remains optically chiral. Scattering and absorption can acquire opposite signs within the same band, requiring circular-polarization-dependent complex output maps rather than one scalar enhancement factor. The complete five-state scattering trajectory is shown in Figure 2.

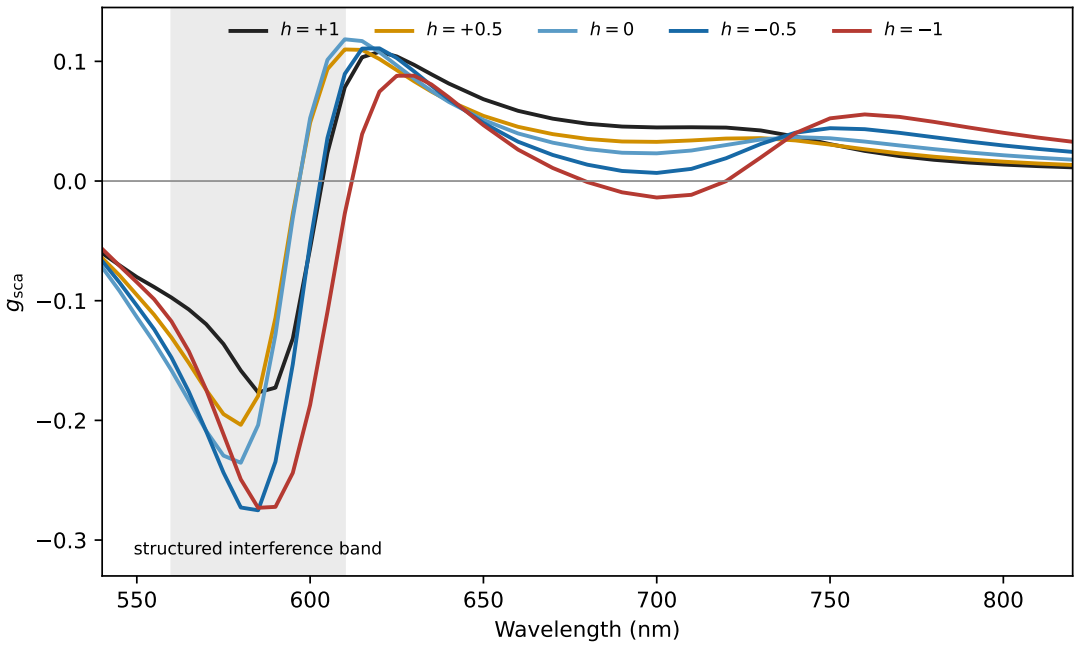


Fig. 2 Five-state linear scattering dissymmetry obtained independently by integrating the full-sphere scattered far field. The pronounced negative branch in the 560–610 nm structured band strengthens as the selected face is counter-wound through $h = -0.5$, while the positive branch evolves non-monotonically. The production cross-section extrema used for the quantitative values in the text are tabulated in Supporting Information Sec. S4.1.

A diagnostic simultaneous two-pole fit to the four raw scattering/absorption channels gives a broad fitted pole near 2.05–2.07 eV with half-width 0.23–0.25 eV and a narrower pole near 1.712–1.722 eV with half-width 0.072–0.080 eV. The fitted pole positions move only modestly with h, whereas dissymmetry changes much more strongly. We therefore use the fit only as a compact representation of residue/background/output-zero motion and do not identify its poles with unique quasinormal modes. Validated five-state cross-section extrema, representative simultaneous fits, and fitted pole trajectories are reported in Supporting Information Sec. S4.

The scalar far-field analysis shows that the fourfold response is strongest near 585–600 nm for most geometries, whereas the planar mean intensity peaks near 730 nm for every h and both incident polarizations. Above approximately 650 nm the normalized pattern becomes comparatively shape invariant. The short-wave angular structure is therefore the geometry- and circular-polarization-sensitive part of the response. Complete scalar anisotropy, orientation, and fourfold-modulation metrics for all five geometries and both circular polarizations are given in Supporting Information Sec. S6.

To determine whether the structured short-wave response is genuinely interference dominated, we use the term Fano-like operationally for a phase-resolved cancellation in a common radiation output produced by coherently overlapping channels with distinct spectral evolution; this terminology does not imply that the resolved radiation channels constitute uniquely identified quasinormal eigenmodes. Here m is the integer azimuthal Fourier index of the radiated field, while σ is the circular-polarization index defined in equation (3). The fourfold face geometry motivates, and the full-sphere calculation below confirms, the modulo-four

channel family

$$m = \sigma + 4q, \qquad q \in \mathbb{Z}. \tag{16}$$

The two largest equatorial Fourier coefficients are consistently the principal member $m = \sigma$ ($q = 0$) and the nearest important secondary member $m = -3\sigma$ ($q = -\sigma$). Thus the dominant pair is $(m = -1, +3)$ for LCP and $(m = +1, -3)$ for RCP. Their index difference is four, which produces the observed fourfold interference term. Retaining them gives

$$\boldsymbol{e} \simeq \boldsymbol{c}_{\sigma} e^{\mathrm{i}\sigma\phi} + \boldsymbol{c}_{-3\sigma} e^{-\mathrm{i}3\sigma\phi}, \tag{17}$$

and the fourfold intensity term

$$I_4(\phi) = 2\,\mathrm{Re}\left[\boldsymbol{c}_{\sigma} \cdot \boldsymbol{c}^{*}_{-3\sigma} e^{\mathrm{i}4\sigma\phi}\right]. \tag{18}$$

Across the five geometries, this two-channel cross term accounts for approximately 98.3–99.2% of the measured complex fourfold coefficient. The weaker branch reaches only 12–18% of the dominant-channel amplitude, yet its interference contribution can be much larger than its standalone power fraction. Figure 3 shows the corresponding complex angular-channel amplitudes and phases. The complete Fourier-channel amplitudes, phases, secondary-to-primary ratios, and reconstruction test are given in Supporting Information Sec. S7.

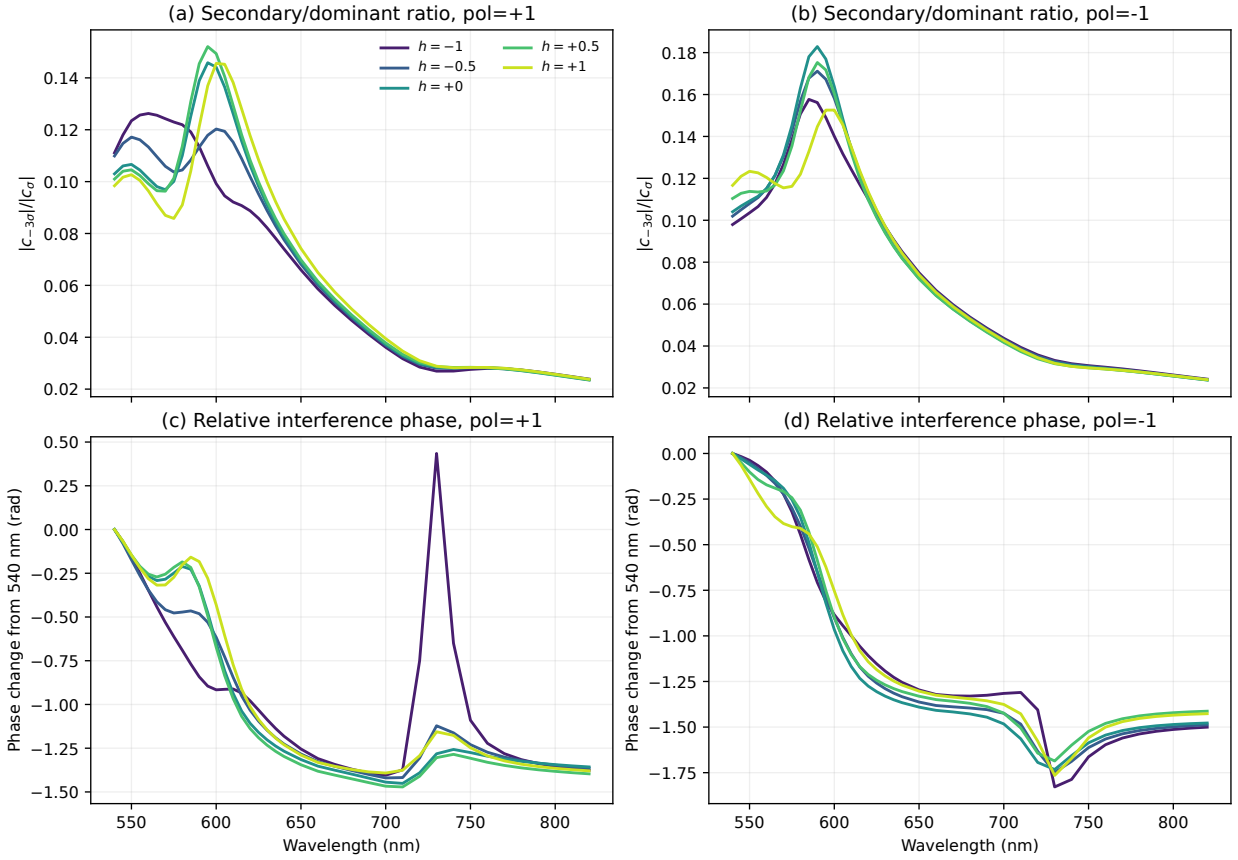


Fig. 3 Complex angular-channel amplitudes and phases. For LCP the principal/secondary pair is $m = -1, +3$, whereas for RCP it is $m = +1, -3$. The weaker $m = -3\sigma$ branch remains small in power but develops sufficient amplitude and phase evolution to reshape the far field through interference.

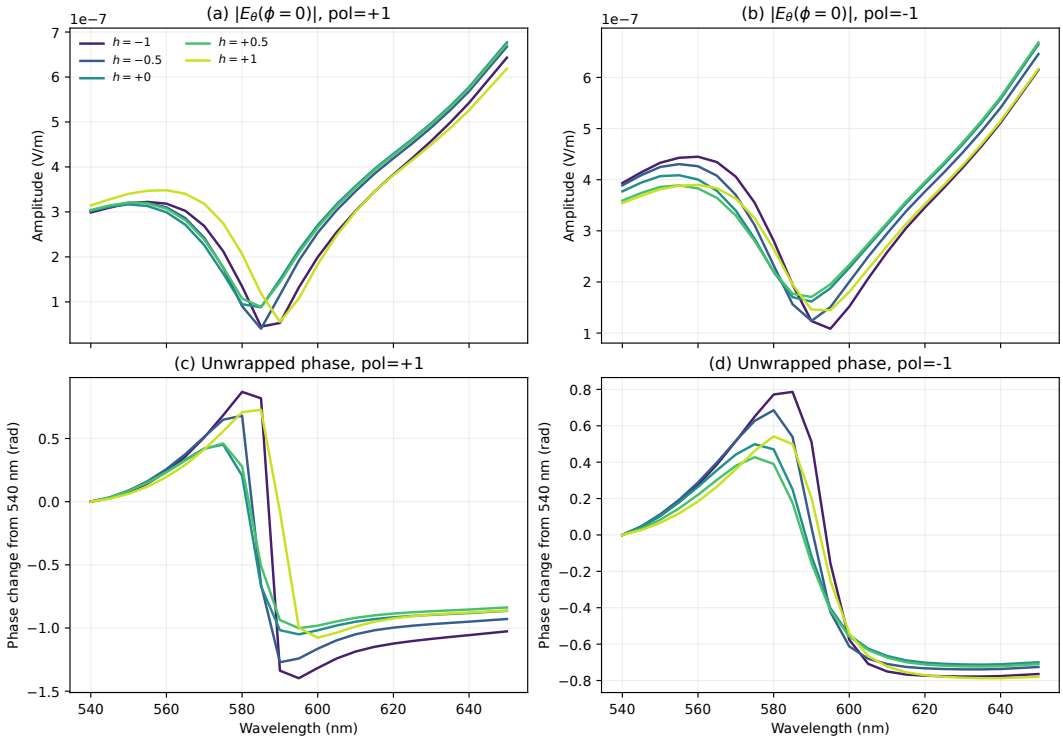


Fig. 4 Fixed-channel amplitude and phase across the five face-helicity states. The physical channel $E_\theta(\phi = 0)$ develops an amplitude minimum near 585–595 nm together with rapid phase evolution, providing a direct phase-resolved signature of the short-wave Fano-like interference.

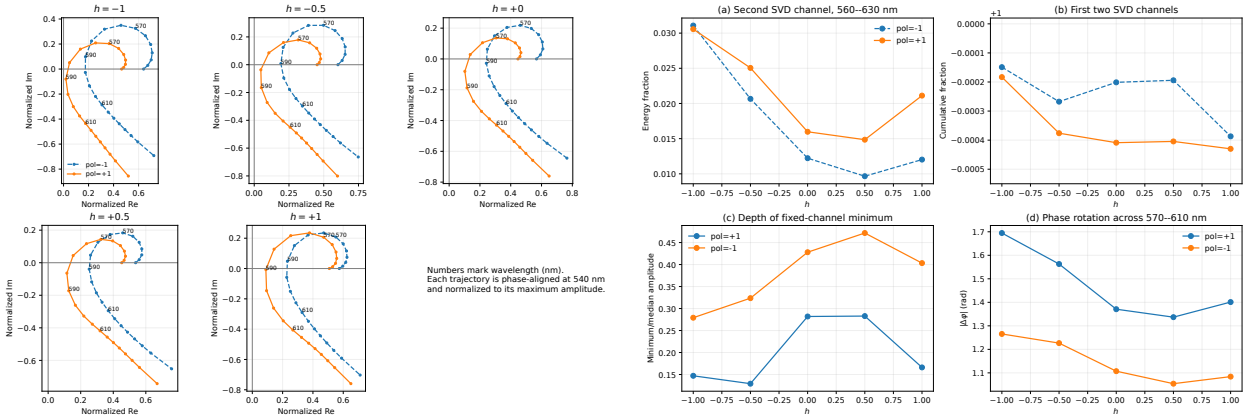
A Fano-like output zero should combine an amplitude minimum with rapid phase evolution. Monitoring the fixed physical channel $E_\theta(\phi = 0)$ gives minima near 585–595 nm for all five h values. Between 570 and 610 nm the phase rotates by approximately 1.34–1.69 rad for RCP and 1.05–1.27 rad for LCP. Figure 4 displays this amplitude-minimum/phase-rotation signature directly; complete fixed-channel trajectories are provided in Supporting Information Sec. S8.

The same cancellation is visible in the complex plane: the corresponding Argand trajectories approach and recover from a cancellation region as wavelength is swept. A basis-independent singular-value decomposition provides an independent low-rank test, with the first two singular channels containing 99.957–99.985% of the complex field energy in the 560–630 nm window. These complementary diagnostics are summarized in Figure 5; full Argand trajectories and SVD diagnostics across the complete h series are provided in Supporting Information Secs. S8 and S9.

The reduced two-channel picture, motivated by temporal coupled-mode descriptions [28], makes the distinction between resonant-pole motion and motion of the measured interference zero explicit. With a_b and a_d denoting the broad and narrower coupled amplitudes, respectively, the radiative output and pole condition may be written compactly as

$$A(\omega, h) = c_{\mathrm{bg}}(h) + c_b(h)a_b(\omega, h) + c_d(h)a_d(\omega, h), \qquad D_b(\omega, h)D_d(\omega, h) - \kappa^2(h) = 0 \quad \text{(poles)}. \tag{19}$$

The observable interference zero instead satisfies $A(\omega_z, h) = 0$ and therefore need not track the poles. Face-helicity variation can therefore change the location and depth of an output minimum through complex excitation



(a) Argand trajectories. **(b)** Low-rank decomposition.

Fig. 5 Complementary phase-resolved diagnostics of the short-wave interference. The Argand trajectories approach and recover from a cancellation region, while the first two singular channels reproduce more than 99.95% of the complex field energy over 560–630 nm.

and radiation weights without requiring comparable changes in the fitted poles. The damped-oscillator derivation of Eq. 19 is given in Supporting Information Sec. S15.

This phase-resolved picture is independently supported by the full-sphere expansion, which confirms the same azimuthal organization. More than 99.995% of the resolved power lies in the family $m = \sigma + 4q$. The secondary $m = -3\sigma$ branch is predominantly electric $\ell = 3$ radiation. For LCP, its maximum total power fraction evolves as 0.925, 1.155, 1.268, 1.145, and 0.967% for $h = +1, +0.5, 0, -0.5, -1$, respectively. At $h = 0$ under LCP illumination, 590 nm, the principal fractions are approximately 73.4% electric dipole, 15.0% electric quadrupole, 9.28% magnetic dipole, and 1.18% in the specific electric-octupole coefficient $(\ell, m) = (3, +3)$. Near 730 nm the magnetic-dipole fraction falls below 0.6% and the radiation becomes almost entirely ED/EQ. Figure 6 summarizes the full-sphere multipole and interference analysis. Coefficient-level results, symmetry-family weights, and the full-sphere fourfold-interference analysis are collected in Supporting Information Sec. S11.

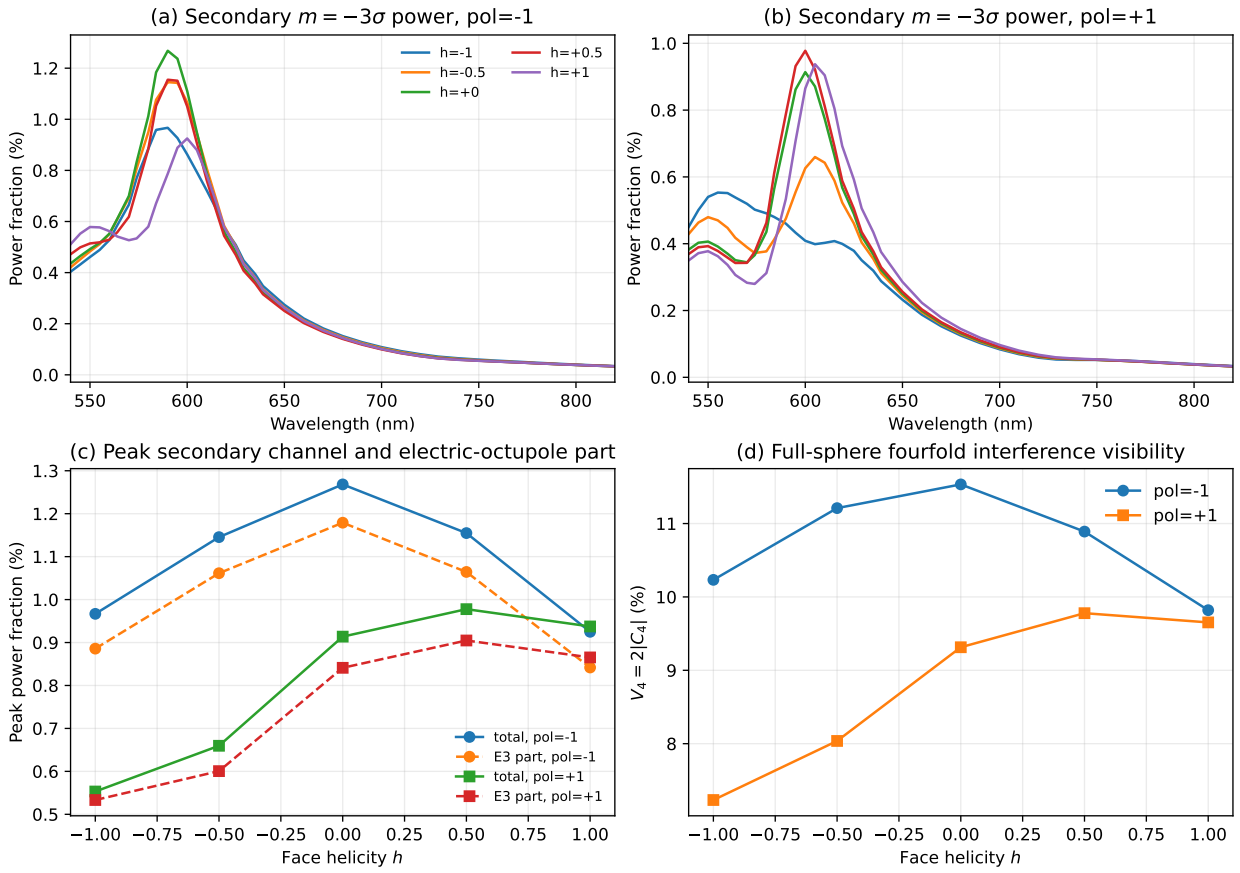


Fig. 6 Full-sphere multipole and interference analysis. The weak secondary branch is predominantly electric octupole, while the full-sphere fourfold visibility quantifies its coherent angular interference with the dominant branch.

The full-sphere fourfold visibility $V_4 = 2|C_4|$ reaches 0.115 for $h = 0$ under LCP illumination near 590 nm. Normal-to-Fine mesh refinement changes the scalar cross sections by at most 0.33% in the short-wave band and leaves the octupolar fraction and V_4 essentially unchanged. A 1-nm sweep places the strongest LCP visibility at 589.86 nm and the electric-octupolar maximum at 591.40 nm. The complex current overlap between 580 and 600 nm remains 0.970 while accumulating 12.8° phase rotation, whereas the 590- and 730-nm current patterns have overlap 0.822 and differ by 55.2°. Detailed Normal-to-Fine and 1-nm wavelength-refinement data and the current-overlap diagnostics are given in Supporting Information Secs. S12 and S13.

Finite numerical aperture projects this angular interference into a directly measurable quantity. For $h = -0.5$ at 580 nm, a 30° cone about $+z$ changes the full-sphere $g = -0.273$ to $g_{+z} = -0.384$ while retaining 25.0% of the radiated power. A large directional $|g|$ is therefore meaningful only together with collected power. The complete collection-angle dependence and the tradeoff between directional dissymmetry and retained power are reported in Supporting Information Sec. S14.

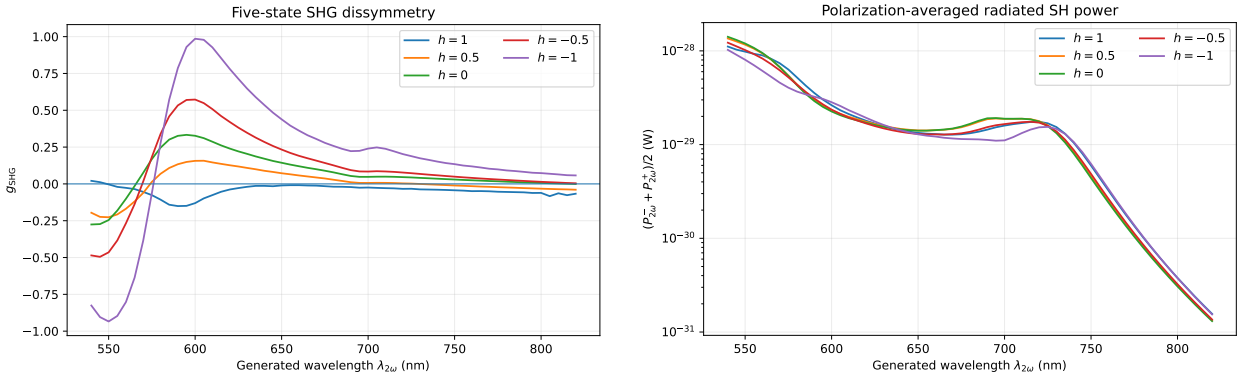
3.2 Nonlinear chiroptical response

Having established a phase-sensitive linear radiation environment near 590 nm, we next examine whether the same generated-frequency region controls the nonlinear response. The five-state SHG series is shown in

figure 7, and the extrema are listed in table 1.

Table 1: Extrema of the five-state surface-SHG series. Wavelengths refer to the generated second harmonic.

h	maximum g_{SHG}	wavelength	minimum g_{SHG}	wavelength
+1	+0.02075	540 nm	−0.15057	590 nm
+0.5	+0.15727	605 nm	−0.22652	550 nm
0	+0.33314	595 nm	−0.27552	540 nm
−0.5	+0.57276	600 nm	−0.49524	545 nm
−1	+0.98582	600 nm	−0.93425	550 nm



(a) g_{SHG} spectra.

(b) Polarization-averaged SH power.

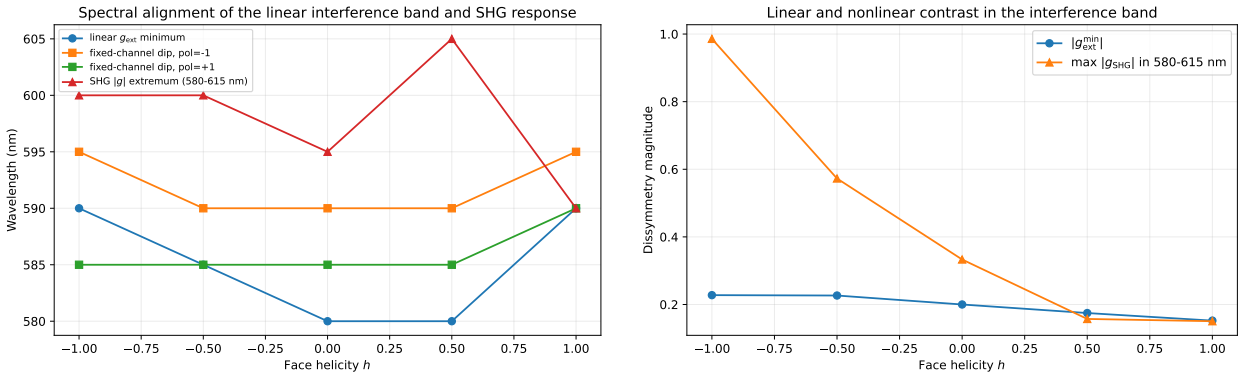
Fig. 7 Nonlinear response of the five-state face-helicity series obtained from the two-step pump-to-SH surface-source calculation. The vertical guide marks $\lambda_{2\omega} = 600$ nm.

At 600 nm the trajectory is

$$g_{\mathrm{SHG}} = (-0.1305,\ 0.1565,\ 0.3269,\ 0.5728,\ 0.9858) \tag{20}$$

for $h = (+1, +0.5, 0, -0.5, -1)$. The $h = -1$ value corresponds to an LCP/RCP SH-power ratio of 2.944. A focused end-to-end Normal-to-Fine mesh test was performed for this headline point, recomputing both 1200-nm pump polarizations and the corresponding 600-nm SH fields on the Fine mesh. The LCP and RCP SH powers change by only −0.71% and +0.34%, respectively, and g_{SHG} changes from 0.9858 to 0.9778. The near-unity nonlinear dissymmetry is therefore robust to mesh refinement. The magnitude of the nonlinear contrast becomes far larger than the scalar linear extinction dissymmetry as the selected face is counter-wound. The machine-readable wavelength-resolved nonlinear spectra underlying figure 7 are documented in Supporting Information Sec. S17, and the focused end-to-end nonlinear convergence test is given in Sec. S18.

The spectral location of this nonlinear evolution provides the first link to the linear interference mechanism. The linear fixed-output minima remain at 585–595 nm for LCP and RCP across all five geometries. The dominant nonlinear extrema in the 580–615 nm interval occur at 590, 605, 595, 600, and 600 nm as h runs from +1 to −1. Thus the large nonlinear evolution occurs without a corresponding large translation of the spectral feature, as summarized in Figure 8.



(a) Linear fixed-channel minima and SHG extrema.

(b) Linear versus nonlinear dissymmetry magnitude.

Fig. 8 Connection between the independently established linear Fano band and the nonlinear response. The generated SH feature remains spectrally locked to the visible interference band while its LCP/RCP contrast grows much more strongly with selected-face reversal.

This observation is important because the pump wavelength associated with 600-nm SH radiation is 1200 nm, whereas the phase-resolved linear Fano evidence is at the generated visible frequency. The coincidence therefore points naturally to the electromagnetic response at 2ω as an important nonlinear amplifier. It does not prove that the same two open-system eigenmodes provide a unique nonlinear basis; rather, it establishes that the nonlinear output is largest where the independently solved visible-frequency particle response is phase sensitive and interference dominated. A geometry-by-geometry comparison of the linear fixed-channel minima, linear extinction extrema, and nonlinear band extrema is given in Supporting Information Sec. S21.

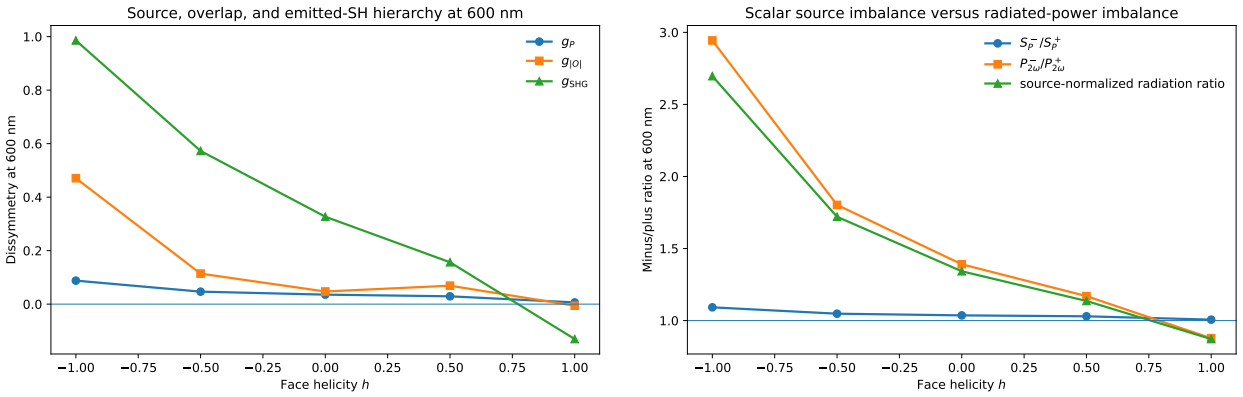
To identify where the large nonlinear asymmetry develops, we next test whether it is already present in the pump-derived source. The source norm provides the cleanest scalar diagnostic. At 600 nm,

$$g_P = (0.0064,\ 0.0292,\ 0.0355,\ 0.0467,\ 0.0879), \tag{21}$$

whereas g_{SHG} reaches 0.9858 for $h = -1$. The source-field overlap diagnostic also changes more strongly than the scalar source norm,

$$g_{|O|} = (-0.0058,\ 0.0690,\ 0.0472,\ 0.1141,\ 0.4707), \tag{22}$$

but it still does not reproduce the emitted SH dissymmetry. Pump-only $|E_\omega|^2$, $|E_\omega|^4$, and signed-normal-field diagnostics at 1200 nm vary substantially less than the SH trajectory and likewise do not account for the nonlinear contrast; these controls are retained in Supporting Information Sec. S20. Figure 9 then compares the source, overlap, and radiated-output levels directly at 600 nm.



(a) Source, overlap, and radiated dissymmetry.

(b) LCP/RCP ratios and source-normalized radiation ratio.

Fig. 9 Nonlinear mechanism diagnostics at a generated wavelength of 600 nm. The integrated source norm remains comparatively weakly circular-polarization selective while the emitted SH power becomes strongly selective. The source-normalized radiation ratio is a diagnostic normalization, not a conversion efficiency.

For $h = -1$ at 600 nm,

$$\frac{S_P^{\mathrm{LCP}}}{S_P^{\mathrm{RCP}}} = 1.092, \qquad \frac{P_{2\omega}^{\mathrm{LCP}}}{P_{2\omega}^{\mathrm{RCP}}} = 2.944, \tag{23}$$

so that

$$\frac{P_{2\omega}^{\mathrm{LCP}}/P_{2\omega}^{\mathrm{RCP}}}{S_P^{\mathrm{LCP}}/S_P^{\mathrm{RCP}}} = 2.70. \tag{24}$$

Across $h = +1, +0.5, 0, -0.5, -1$, this source-normalized radiation ratio evolves approximately as 0.872, 1.136, 1.342, 1.720, and 2.696. The result rules out a purely scalar source-strength interpretation. The complete five-state source-norm, overlap-magnitude, and radiated-power hierarchy is given in Supporting Information Sec. S19.

An even stronger diagnostic occurs for $h = -1$ at 550 nm. There $g_P = +0.0959$ and $g_{|O|} = +0.3807$, yet the emitted value is $g_{\mathrm{SHG}} = -0.9343$. The radiation therefore can reverse the LCP/RCP preference suggested by both scalar source magnitude and overlap magnitude. Relative spatial phase, vector orientation, and the 2ω Green response are indispensable. The numerical sign-reversal test is detailed in Supporting Information Sec. S19.3.

This mechanism is analogous to Fano-enhanced nonlinear response in the sense emphasized in earlier coupled-mode work [23]: coherent interference allows the nonlinear output to change far more strongly than a scalar measure of the drive. The present numerical evidence, however, locates the most compelling enhancement at the generated-frequency radiation stage. We therefore do not claim that the nonlinear g factor is simply the square of the linear response or that one fitted two-mode numerator uniquely describes the full-wave numerical data. A heuristic nonlinear coupled-mode extension illustrating where coherent source-level and generated-frequency interference can enter is given in Supporting Information Sec. S22.

Taken together, the linear and nonlinear results support a generated-frequency interpretation. The linear Fano assignment is made at the directly resolved radiation-channel level: a fixed output amplitude approaches a minimum while its phase rotates; the field is low rank; a weak predominantly electric-octupolar branch coherently redistributes radiation with a dominant mixed branch; and the feature is stable under mesh and wavelength refinement. The nonlinear result is a second, distinct statement. The nonlinear source is only

weakly circular-polarization selective in scalar norm, while the generated SH field acquires much stronger and even sign-reversed LCP/RCP selectivity within the same visible interference band. The data therefore support the chain

$$\boldsymbol{E}_{\omega} \longrightarrow \boldsymbol{P}_{s}^{(2)} \longrightarrow \text{phase-sensitive coupling/radiation at } 2\omega \longrightarrow P_{2\omega}, \tag{25}$$

with the strongest chirality developing after source formation.

Uniform size rescaling provides a useful negative control: it can move the long-wavelength response toward the experimental feature near 723 nm, but it cannot simultaneously align the short-wave feature over the tested 150–180 nm size range. The size calibration and a digitized comparison with the NP0 data of Spreyer *et al.* [10] are given in Supporting Information Secs. S5.1 and S5.2.

Comparison with experiment requires raw intensities rather than direct averaging of g. For a structural mixture,

$$I_{\mathrm{ens}}^{(s)}(\lambda) = \sum_{h} w_h I_{h}^{(s)}(\lambda), \qquad w_h \geq 0, \quad \sum_{h} w_h = 1, \tag{26}$$

followed by formation of g from the mixed intensities. Substrate, orientation distribution, size dispersion, and collection geometry must be included similarly. The present connected helicoid-III-inspired geometry is therefore a controlled mechanism model rather than a quantitative reconstruction of one experimental ensemble.

Several limitations define the scope of this interpretation. The linear interference assignment was tested independently against both spatial and spectral discretization. For the $h = 0$ geometry, a physics-controlled Normal-to-Fine mesh refinement changes the scattering, absorption, and extinction cross sections by at most 0.326%, 0.099%, and 0.127%, respectively, within the structured short-wave band, while the fourfold visibility and electric-octupolar fraction at 590 nm remain essentially unchanged. An independent 1-nm wavelength sweep from 575 to 605 nm likewise preserves the locations and interpretation of the phase-sensitive interference landmarks. Complete linear mesh- and wavelength-convergence results are given in Supporting Information Sec. S12. These focused tests establish numerical stability of the representative linear Fano-like assignment, although a Fine-mesh sweep over every geometry and wavelength was not attempted.

The full-sphere VSH and finite-cone calculations use approximately 5° angular sampling, with the $\ell_{\max} = 8$ reconstruction converged at the 1.5×10^{-4} level. Radiation multipoles are not automatically quasinormal modes, and the two-pole scalar fit remains diagnostic rather than a unique eigenmode extraction. Absolute SH powers depend on the chosen effective surface susceptibility and its local normal–tangential implementation; the principal nonlinear conclusions instead rely on relative polarization and geometry trends obtained using one common source model. A focused nonlinear Normal-to-Fine convergence test at the strongest positive-dissymmetry point, $h = -1$ and $\lambda_{2\omega} = 600$ nm, recomputes both the 1200-nm pump field and the SH field on the Fine mesh. The resulting dissymmetry changes only from $g_{\mathrm{SHG}} = 0.9858$ to 0.9778, while each of the two SH powers changes by less than 1%. Complete nonlinear convergence data are given in Supporting Information Sec. S18. This establishes mesh robustness of the headline near-unity nonlinear response, while a systematic nonlinear Fine-mesh sweep over every geometry and wavelength remains outside the present scope.

4 Conclusion

A controlled change in the winding of one connected face is sufficient to reorganize the chiroptical radiation of an otherwise fixed left-handed gold helicoid without simply translating a single resonance. In the structured 560–610 nm linear band, a dominant $m = \sigma$ radiation channel interferes with a weaker $m = -3\sigma$ branch that is predominantly electric octupole. Fixed-channel amplitude minima and rapid phase rotation, low-rank complex fields, full-sphere fourfold visibility, induced-current evolution, and numerical refinement provide mutually consistent evidence for Fano-like coherent-radiation interference. The broad response near 730 nm is physically distinct and largely ED/EQ, showing that the complete spectrum should not be reduced to a single two-mode line shape.

Independent geometry controls reinforce the interference-based interpretation. Terminating the reference grooves before the rounded edges leaves the polarization-averaged scattering maximum nearly unchanged while substantially reorganizing g_{sca}, demonstrating that inter-face current continuity can change helicity-sensitive radiation without simply increasing overall scattering strength. More strikingly, the shallow edge-touching $D = 0.25$ control retains a strong average scattering resonance while suppressing $|g_{\mathrm{sca}}|$ below approximately 3×10^{-3}. Strong plasmonic scattering is therefore not sufficient for strong chiroptical response; local winding, depth, and connectivity regulate the coherent amplitudes and phases that determine the helicity-sensitive output.

The nonlinear calculation extends this picture to frequency conversion. At a generated wavelength of 600 nm, g_{SHG} evolves from -0.131 to $+0.986$ as the selected face changes from $h = +1$ to $h = -1$, while the nonlinear-source-norm dissymmetry grows only from 0.0064 to 0.0879. For $h = -1$, a source ratio of 1.092 becomes a radiated-power ratio of 2.944, corresponding to a source-normalized radiation ratio of 2.70. At 550 nm, the emitted SH preference even reverses relative to both the source-norm and overlap-magnitude diagnostics. These results show that scalar pump enhancement and scalar source magnitude do not determine the nonlinear chirality; relative phase, vectorial source structure, and the electromagnetic Green response at 2ω are essential. The headline $h = -1$, 600-nm result is also numerically stable: an end-to-end Fine-mesh recalculation changes the two SH powers by less than 1% and g_{SHG} from 0.9858 to 0.9778.

The dominant nonlinear extrema remain in the 590–605 nm generated-wavelength interval, coincident with the independently established visible-frequency Fano band. We therefore interpret selected-face reversal primarily as a reweighting of the complex coupling between the surface nonlinear polarization and a phase-sensitive radiation environment at 2ω, rather than as a large shift of a nonlinear resonance. From a nanoscale design perspective, this is the central opportunity: local winding and inter-face connectivity provide a compact structural handle for tuning helicity-selective output while the gross plasmonic resonance remains comparatively fixed. Such local control could be implemented through growth variation, selective overgrowth or etching, or post-fabrication modification of individual facets. The generated-frequency viewpoint thus suggests a route to interference-controlled nonlinear chiroptical functionality without requiring wholesale redesign of the particle, and motivates experiments that jointly resolve nonlinear polarization contrast, angular radiation, and local morphology.

Acknowledgements

This work was carried out during G.B.A.'s research visit to the Department of Physics at Prairie View A&M University, Prairie View, Texas, USA. The authors thank Mehmet Emre Tasgin for valuable initial discussions.

Supplementary Information

Online Resource 1: Supporting Information containing geometry and polarization controls, size and experimental-comparison diagnostics, phase and multipole tables, convergence and current diagnostics, finite-collection analysis, surface-SHG implementation, nonlinear source/overlap diagnostics, and reduced coupled-oscillator derivations.

Online Resource 2: Machine-readable archive of 34 derived numerical tables and analysis-ready postprocessing outputs, with a file inventory.

References

[1] Hye-Eun Lee et al. "Amino-acid- and peptide-directed synthesis of chiral plasmonic gold nanoparticles". In: *Nature* 556 (2018), pp. 360–365. DOI: 10.1038/s41586-018-0034-1.

[2] Jeong Won Kim et al. "Controlling the size and circular dichroism of chiral gold helicoids". In: *Materials Advances* 2 (2021), pp. 6988–6995. DOI: 10.1039/D1MA00783A.

[3] Jeong Hyun Han et al. "Isotropic Size Control of Chiral Gold Helicoids". In: *The Journal of Physical Chemistry C* 129.14 (2025), pp. 7020–7030. DOI: 10.1021/acs.jpcc.4c08606.

[4] Julian Karst et al. "Chiral Scatterometry on Chemically Synthesized Single Plasmonic Nanoparticles". In: *ACS Nano* 13.8 (2019), pp. 8659–8668. DOI: 10.1021/acsnano.9b04046.

[5] Patrick Spaeth et al. "Photothermal Circular Dichroism Measurements of Single Chiral Gold Nanoparticles Correlated with Electron Tomography". In: *ACS Photonics* 9.12 (2022), pp. 3995–4004. DOI: 10.1021/acsphotonics.2c01457.

[6] Jeong Won Kim et al. "Magnetic Control of the Plasmonic Chirality in Gold Helicoids". In: *Nano Letters* 22.20 (2022), pp. 8181–8188. DOI: 10.1021/acs.nanolett.2c02661.

[7] Jian Yang et al. "Unraveling the Origin of Reverse Plasmonic Circular Dichroism from Discrete Bichiral Au Nanoparticles". In: *Nano Letters* 24.37 (2024), pp. 11706–11713. DOI: 10.1021/acs.nanolett.4c03331.

[8] Xiali Lv et al. "Chiral Plasmonic–Dielectric Coupling Enables Strong Near-Infrared Chiroptical Responses from Helicoidal Core–Shell Nanoparticles". In: *Nature Communications* 15 (2024), p. 9234. DOI: 10.1038/s41467-024-53705-4.

[9] Lukas Ohnoutek et al. "Single nanoparticle chiroptics in a liquid: Optical activity in hyper-Rayleigh scattering from Au helicoids". In: *Nano Letters* 20.8 (2020), pp. 5792–5798. DOI: 10.1021/acs.nanolett.0c01659.

[10] Florian Spreyer et al. "Second-Harmonic Optical Circular Dichroism of Plasmonic Chiral Helicoid-III Nanoparticles". In: *ACS Photonics* 9.3 (2022), pp. 784–792. DOI: 10.1021/acsphotonics.1c00882.

[11] E. A. Mamonov et al. "Anisotropy versus Circular Dichroism in Second Harmonic Generation from Fourfold Symmetric Arrays of G-Shaped Nanostructures". In: *Physical Review B* 89.12 (2014), p. 121113. DOI: 10.1103/PhysRevB.89.121113.

[12] Radoslaw Kolkowski et al. “Octupolar Plasmonic Meta-Molecules for Nonlinear Chiral Watermarking at Subwavelength Scale”. In: *ACS Photonics* 2.7 (2015), pp. 899–906. DOI: 10.1021/acsphotonics.5b00090.

[13] Joel T. Collins et al. “Second-Harmonic Generation Optical Rotation Solely Attributable to Chirality in Plasmonic Metasurfaces”. In: *ACS Nano* 12.6 (2018), pp. 5445–5451. DOI: 10.1021/acsnano.8b00601.

[14] Lili Gui et al. “Nonlinear Born–Kuhn Analog for Chiral Plasmonics”. In: *ACS Photonics* 6.12 (2019), pp. 3306–3314. DOI: 10.1021/acsphotonics.9b01400.

[15] Ben J. Olohan et al. “Second-Harmonic Chiroptical Scattering Spectroscopy from Plasmonic Nanohelices”. In: *Optics Express* 34.8 (2026), pp. 14662–14672. DOI: 10.1364/OE.582687.

[16] Guillaume Bachelier et al. “Origin of Optical Second-Harmonic Generation in Spherical Gold Nanoparticles: Local Surface and Nonlocal Bulk Contributions”. In: *Physical Review B* 82.23 (2010), p. 235403. DOI: 10.1103/PhysRevB.82.235403.

[17] Daniel Timbrell et al. “A Comparative Analysis of Surface and Bulk Contributions to Second-Harmonic Generation in Centrosymmetric Nanoparticles”. In: *Scientific Reports* 8 (2018), p. 3586. DOI: 10.1038/s41598-018-21850-8.

[18] Ugo Fano. “Effects of configuration interaction on intensities and phase shifts”. In: *Physical Review* 124.6 (1961), pp. 1866–1878. DOI: 10.1103/PhysRev.124.1866.

[19] Boris Lukyanchuk et al. “The Fano resonance in plasmonic nanostructures and metamaterials”. In: *Nature Materials* 9 (2010), pp. 707–715. DOI: 10.1038/nmat2810.

[20] Shanhui Fan, Wonjoo Suh, and John D. Joannopoulos. “Temporal coupled-mode theory for the Fano resonance in optical resonators”. In: *Journal of the Optical Society of America A* 20.3 (2003), pp. 569–572. DOI: 10.1364/JOSAA.20.000569.

[21] Andrea Lovera et al. “Mechanisms of Fano resonances in coupled plasmonic systems”. In: *ACS Nano* 7.5 (2013), pp. 4527–4536. DOI: 10.1021/nn401175j.

[22] Yongsop Hwang et al. “Effects of Fano Resonance on Optical Chirality of Planar Plasmonic Nanodevices”. In: *ACS Photonics* 5.11 (2018), pp. 4538–4544. DOI: 10.1021/acsphotonics.8b01007.

[23] Deniz Turkpence et al. “Engineering nonlinear response of nanomaterials using Fano resonances”. In: *Journal of Optics* 16.10 (2014), p. 105009. DOI: 10.1088/2040-8978/16/10/105009.

[24] Jérémy Butet and Olivier J. F. Martin. “Fano Resonances in the Nonlinear Optical Response of Coupled Plasmonic Nanostructures”. In: *Optics Express* 22.24 (2014), pp. 29693–29707. DOI: 10.1364/OE.22.029693.

[25] Sushmita Biswas et al. “Nonlinear Chiro-Optical Amplification by Plasmonic Nanolens Arrays Formed via Directed Assembly of Gold Nanoparticles”. In: *Nano Letters* 15.3 (2015), pp. 1836–1842. DOI: 10.1021/nl504613q.

[26] Patrick Grahn, Andriy Shevchenko, and Matti Kaivola. “Electromagnetic Multipole Theory for Optical Nanomaterials”. In: *New Journal of Physics* 14.9 (2012), p. 093033. DOI: 10.1088/1367-2630/14/9/093033.

[27] P. B. Johnson and R. W. Christy. “Optical Constants of the Noble Metals”. In: *Physical Review B* 6.12 (1972), pp. 4370–4379. DOI: 10.1103/PhysRevB.6.4370.

[28] Wonjoo Suh, Zheng Wang, and Shanhui Fan. “Temporal coupled-mode theory and the presence of non-orthogonal modes in lossless multimode cavities”. In: *IEEE Journal of Quantum Electronics* 40.10 (2004), pp. 1511–1518. DOI: 10.1109/JQE.2004.834773.

Statements and Declarations

Funding

G.B.A. acknowledges support from the Scientific and Technological Research Council of Türkiye (TÜBİTAK) through the 2219 International Postdoctoral Research Fellowship Program for Turkish Citizens (Project No. 1059B192500156).

Author Contributions

G.B.A. performed the numerical simulations and postprocessing and prepared the initial manuscript. O.C. contributed to scientific discussion, interpretation, and manuscript revision. Both authors reviewed the results, approved the final manuscript, and accept responsibility for its content.

Competing Interests

The authors declare no conflict of interest.

Research Ethics

Not applicable. This computational study involves no human participants, animals, or clinical data.

Data Availability Statement

Derived numerical tables and analysis-ready postprocessing outputs are supplied as Online Resource 2; the accompanying methods and diagnostics are provided in Online Resource 1. Large raw field exports are available from the corresponding author upon reasonable request.

Use of AI tools

During August–September 2026, OpenAI ChatGPT (GPT-5.6 Sol) was used for language editing, manuscript organization, assistance with numerical postprocessing workflows, LaTeX formatting, and drafting of figure layouts. It was not used to generate or alter the underlying simulation data. All AI-assisted text and organizational suggestions, numerical results, equations, references, figures, interpretations, and conclusions were checked against the original simulation outputs and source literature and were reviewed and verified by the authors, who take responsibility for the submitted content. No sensitive human-subject or proprietary personal data were provided to the AI system. OpenAI ChatGPT was also used in October–November 2026 to assist with journal-specific editorial adaptation, LaTeX formatting, and preparation of submission documents; the underlying simulation data were not changed.

Supplementary Files

This is a list of supplementary files associated with this preprint. Click to download.

- ESM2.zip
- ESM1.pdf